remote sensing

MDPI

Article

Evaluation of the Predictive Capability of CMA Climate Prediction System Model for Summer Surface Heat Source on the Tibetan Plateau

Xinyu Chen [1], Minhong Song [1,*], Yaqi Wang [1] and Tongwen Wu [2]

[1] Plateau Atmosphere and Environment Key Laboratory of Sichuan Province, School of Atmospheric Sciences, Chengdu University of Information Technology, Chengdu 610225, China; cxy18116544991@outlook.com (X.C.); 3230101080@stu.cuit.edu.cn (Y.W.)
[2] Earth System Numerical Prediction Center, China Meteorological Administration, Beijing 100081, China
* Correspondence: songmh@cuit.edu.cn

Abstract: Surface heat source (SHS) is a crucial factor affecting local weather systems. Particularly SHS on the Tibetan Plateau (TP) significantly influences East Asian atmospheric circulation and global climate. Accurate prediction of summer SHS on the TP is of urgent demand for economic development and local climate change. To evaluate the performance of SHS on the TP, the observed SHS data from the eleven sites on the TP verified against CRA40-land (CRA) is evidenced significantly better than ERA5-land (ERA5), another widely used reanalysis. The predictive capability of the CMA Climate Prediction System Model (CMA-CPS) for SHS on the TP was assessed using multiple scoring methods, including the anomaly correlation coefficient and temporal correlation coefficient, among others. Furthermore, relative variability and trend analysis were conducted. Finally, based on these assessments, the causes of the biases were preliminarily discussed. The CMA-CPS demonstrates a reasonable ability to predict the spatial distribution patterns of SHS, sensible heat (SH), and latent heat (LH) on the TP in summer. Specifically, the prediction results of SHS and LH exhibit an "east-high and west-low" distribution, while the distribution of the predicted SH is opposite. Nevertheless, the predicted values are generally lower than CRA, particularly in interannual variations and trends. Among the predictions, LH exhibits the highest temporal correlation coefficients, consistently above 0.6, followed by SHS, while SH predictions are less accurate. The spatial distribution and skill scores indicate that LH on the TP contributes more significantly to SHS than SH in summer. Furthermore, discrepancies in the predictions of surface temperature gradients, ground wind speed, and humidity on the TP may partly explain the biases in SHS and their components.

Keywords: Tibetan Plateau; CMA Climate Prediction System Model; surface heat source; predictive capability

check for updates

Citation: Chen, X.; Song, M.; Wang, Y.; Wu, T. Evaluation of the Predictive Capability of CMA Climate Prediction System Model for Summer Surface Heat Source on the Tibetan Plateau. *Remote Sens.* **2024**, *16*, 4118. https://doi.org/10.3390/rs16214118

Academic Editor: Carmine Serio

Received: 26 August 2024
Revised: 16 October 2024
Accepted: 1 November 2024
Published: 4 November 2024

Copyright: © 2024 by the authors. Licensee MDPI, Basel, Switzerland. This article is an open access article distributed under the terms and conditions of the Creative Commons Attribution (CC BY) license (https://creativecommons.org/licenses/by/4.0/).

1. Introduction

The Tibetan Plateau (TP) is the highest plateau in the world, with an average elevation exceeding 4000 m, earning it the titles "Roof of the World" and "Third Pole". The surface of the TP is situated in the middle troposphere, and its strong thermal effects in summer significantly influence the atmospheric circulation, monsoons, precipitation patterns in East Asia, and global climate [1–4]. Consequently, the thermal effects and SHS over the TP in summer have been extensively studied [5–9].

SH and LH are critical components of SHS, particularly in complex regions such as TP. Numerous studies have sought to estimate SH using observational station data combined with bulk transfer formulas. These studies have highlighted interannual variation trends and seasonal transition characteristics of SH in TP environments [10–12]. In particular, Yang et al. [13] proposed a physical scheme for estimating the daily average SH based on data from China Meteorological Administration stations. However, the uneven distribution

of these stations across the TP often results in an overestimation of SH. Conversely, LH is predominantly analyzed using reanalysis data, with observational station precipitation data utilized as validation tools. This approach has highlighted a significant correlation between LH in the TP and precipitation patterns across China [14–17]. Recent advancements in observational technology have significantly enhanced research on SHS over the TP, utilizing reanalysis data, satellite data [18–23], and model simulation results [24–30]. Multiple reanalysis datasets were assessed alongside observational station data by Chen et al. [19] and Wu et al. [20], concluding that the ERA-Interim reanalysis data most accurately represented the climatic distribution and seasonal variations of SH on the TP.

The CMA Climate Prediction System Model (CMA-CPS), developed by the National Climate Center of the China Meteorological Administration, has been widely implemented and has generated significant social benefits and international impact [31]. Current evaluations of this prediction model primarily focus on atmospheric circulation, precipitation, temperature, extreme events, marine heatwaves, and greening trends on the TP, largely relying on the consistent dynamic framework of the CMA-CSM model [32–39]. Recent research has made significant strides in enhancing climate prediction capabilities for East Asia, particularly regarding summer precipitation and circulation patterns. Notably, one study focused on seasonal predictions of summer precipitation in the middle-lower reaches of the Yangtze River using the NUIST-CFS1 framework, aiming to improve forecasting accuracy and facilitate effective water resource management [40]. In parallel, another investigation explored the abilities of seasonal prediction models to capture East Asian summer circulation and their responses to tropical oceanic changes, elucidating critical mechanisms influencing the regional climate [41]. Furthermore, the ECCC monthly forecasting system demonstrated robust capabilities for sub-seasonal predictions, effectively capturing boreal summer climate variations and examining performance across various climate patterns [42]. Complementarily, an assessment of the Community Earth System Model—Large Ensemble CESM−LE highlighted notable uncertainties in simulating temperature and precipitation trends, particularly extreme values, underscoring the significance of understanding these uncertainties for reliable climate predictions and strategic planning [43]. Lastly, research within the Sub-seasonal to Seasonal Prediction Project database evaluated multiple climate models for their capacity to simulate the Asian summer monsoon's intensity, duration, and spatial distribution, revealing significant model discrepancies that warrant further investigation to enhance sub-seasonal forecasting accuracy [44]. Together, these findings highlight the critical role of improving climate prediction models in understanding the East Asian climate system. The diverse frameworks and methodologies examined, including the NUIST-CFS1 and ECCC monthly forecasting system, reveal both strengths and uncertainties. However, relatively limited attention has been given to the SHS and its components. Based on SHS over the TP playing a critical role in influencing the weather and climate of East Asia and worldwide, this study aims to bridge this gap in accurate prediction. By utilizing measured SHS data over the TP, a comprehensive comparison is made between ERA5 and CRA reanalysis data. The prediction capability of CMA-CPS specifically for SHS over the TP in summer is assessed using various evaluation methods. Furthermore, this study seeks to identify potential reasons for any observed prediction biases, which will provide essential insights for enhancing and refining the CMA-CPS. Ultimately, the results aim to contribute to a better understanding of surface heat dynamics over the TP, which are crucial for improving climate prediction models and their applications.

2. Data and Methods

2.1. Data Description

The site data are provided by the National Tibetan Plateau Data Center, which offers a high-resolution (hourly) comprehensive observation dataset of land-atmosphere interaction processes on the TP. This dataset includes 12 field observation stations distributed across different regions of the TP, covering typical TP surface types such as alpine meadows, alpine steppes, desert gobi, desert steppes, mountain forests, and TP lakes, effectively representing

the complex surface types over the TP [45]. Detailed information about each observation station can be found in the study [45]. Based on the completeness and geographical location of the observation station data, eleven stations, excluding the MAWORS station, were selected. The selected period is July and August of each year from the establishment of the stations up to 2020.

The prediction data come from the third-generation sub-seasonal to seasonal to interannual integrated climate model prediction system developed by the National Climate Center of the China Meteorological Administration. In recent years, the National Climate Center has made significant progress in model development, with new versions including the Earth System Model BCC-ESM1.0, the medium-resolution climate system model BCC-CSM2-MR, and the high-resolution climate system model BCC-CSM2-HR [46]. All three models include four components: atmosphere, land surface, ocean, and sea ice. BCC-CSM2-HR has successfully addressed scientific issues related to vertical resolution and the stratosphere by improving multiple physical process parameterization schemes, developing ensemble prediction methods, and establishing the CMA-CPS. The resolution of each subsystem module has been enhanced and optimized, with the atmospheric model reaching 0.45° × 0.45°, vertical height extending from 40 km to 65 km, and the ocean model's horizontal resolution improving to 0.25° × 0.25° with a vertical depth of 5.5 km. This study utilizes SHS data with a horizontal resolution of 0.45° × 0.45°, predicted by the CMA-CPS starting in May for the summer months from 2001 to 2021, analyzed on both a monthly and daily basis. At the same time, reanalysis data with a horizontal resolution of 0.1° × 0.1° from ERA5 provided by the European Centre for Medium-Range Weather Forecasts (ECMWF) and reanalysis data with a horizontal resolution of 0.25° × 0.25° from CRA provided by the National Meteorological Information Center of the China Meteorological Administration were selected for the same period.

Using a direct algorithm [47], the SH and LH over the TP were summed to obtain the SHS for the corresponding period. For ease of evaluation, all grid point data were uniformly processed to a horizontal resolution of 0.5° × 0.5°.

2.2. Methods

The skill score methods used include [48–50] anomaly correlation coefficient (*ACC*) and temporal correlation coefficient (*TCC*), which, respectively, reflect the spatial similarity between predicted and observed values and better characterize the model's ability to forecast anomalies at each grid point. In this paper, *ACC* scores with positive values and *TCC* scores greater than 0.4 are defined as high-skill scores. Mean Absolute Error (*MAE*) describes the average absolute deviation between predicted and observed values; correlation coefficient (*r*) describes the degree of correlation between predicted and observed values; Root Mean Square Error (*RMSE*) describes the deviation between predicted and observed values; and Relative Root Mean Square Error (*RRMSE*) describes the degree of deviation between predicted and observed values. Additionally, relative variability (the ratio of standard deviation to the absolute value of the mean) [50] and trend rates are used to analyze their trends [11].

The formulas for each skill score method are as follows:

$$ACC = \frac{\sum_{i=1}^{m} (\Delta f_i - \Delta\overline{f_i})(\Delta o_i - \Delta\overline{o_i})}{\sqrt{\sum_{i=1}^{m} (\Delta f_i - \Delta\overline{f_i})^2 \sum_{i=1}^{m} (\Delta o_i - \Delta\overline{o_i})^2}} \quad (1)$$

$$TCC = \frac{\sum_{i=1}^{m} (o_i - \bar{o}_i)(f_i - \bar{f}_i)}{\sqrt{\sum (o_i - \bar{o}_i)^2 \sum (f_i - \bar{f}_i)^2}} \quad (2)$$

$$MAE = \frac{1}{M}\sum_{i=1}^{m}|f_i - o_i| \tag{3}$$

$$RRMSE = \frac{\sqrt{\sum_{i=1}^{m}(o_i - f_i)^2}}{\overline{o_i}} \tag{4}$$

$$r = \frac{\sum_{i=1}^{m}(o_i - \overline{o_i})(f_i - \overline{f_i})}{\sum_{i=1}^{m}(o_i - \overline{o_i})^2(f_i - \overline{f_i})^2} \tag{5}$$

$$RMSE = \sqrt{\frac{1}{m}\sum_{i=1}^{m}(f_i - o_i)^2} \tag{6}$$

In the formula, f and o represent the predicted value and the observed value, respectively. i denotes the sample grid point, and N is the total number of grid points participating in the evaluation.

3. Results

3.1. Model Simulation Evaluation

Figure 1 shows the correlation coefficients (r), root mean square errors ($RMSE$), and standard deviation ratios (SD) between the daily heat flux observation data from 11 observation stations on the TP during July–August and the data from ERA5, CRA, and CMA-CPS. For SH, the site number of positive correlations for CRA is shown at 7 sites, while that for ERA5 is at 9 sites, with overall r values ranging between 0.1 and 0.3. The best correlation for CRA is at NAMORS, approaching 0.4. The RMSE for CRA ranges between 0.8 and 1.6 W/m^2, with standard deviation ratios close to 1. The RMSE for ERA5 is greater than 1.6 W/m^2, with SD generally between 1.5 and 3. For LH, both CRA and ERA5 show positive correlations at 7 sites, with overall r values between 0.1 and 0.3. The best correlation for CRA is at QOMS, approaching 0.4. The RMSE for CRA ranges between 0.8 and 2 W/m^2, with SD generally between 1 and 2; ERA5 shows RMSE greater than 2 W/m^2 at 4 sits, with SD also greater than 2 at 4 stations. For SHS, the correlation indices for CRA and ERA5 are relatively poor compared to SH and LH, with overall r values between 0.06 and 0.28 but with considerable dispersion. For the CMA-CPS, although the dispersion is comparable to that of CRA, the number of positive correlations ranges from 5 to 7, and overall r values lie between 0 and 0.17. The correlation is generally weak in Figure 1, possibly due to the complex environment and harsh climate conditions. However, in some years, the r values exceed 0.5, reaching up to 0.61 (SH in 2008 of CRA at QOMS). Overall, the r values for CRA are slightly better than those for ERA5, with significantly less dispersion. Therefore, CRA is selected as the comparative data to evaluate the prediction ability of the CMA-CPS on the TP.

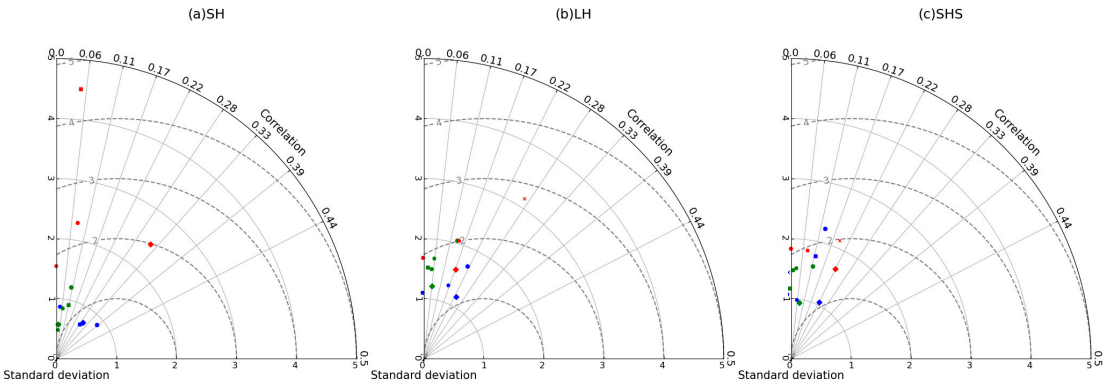


Figure 1. *Cont.*

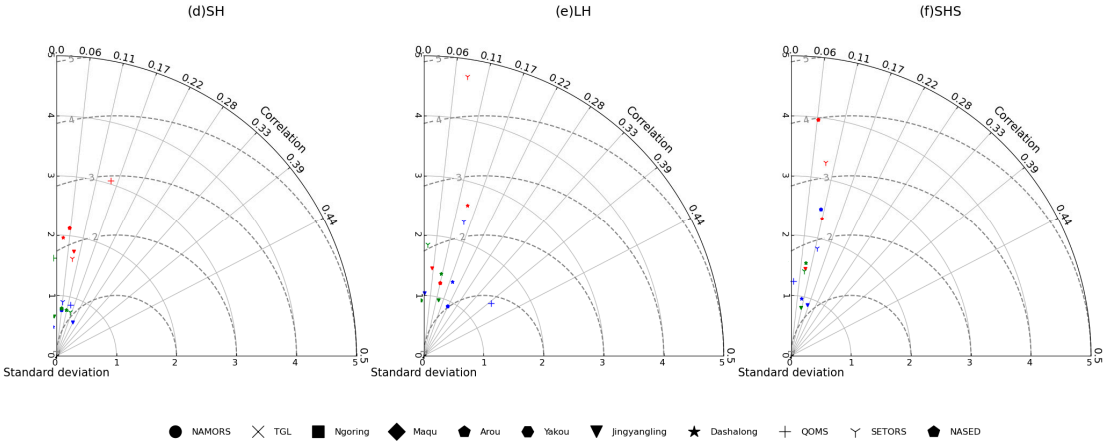


Figure 1. Taylor diagrams of SH (**a**,**d**), LH (**b**,**e**), and SHS (**c**,**f**) from different data sources at 11 observation stations on the TP during July–August. Red represents ERA5 data, blue represents CRA data, green represents CMA−CPS data, and the dashed line indicates the root mean square error.

3.2. Evaluation of Predictive Capability for SH

According to the CMA-CPS predictions, the spatial distribution of summer SH on the TP exhibits a pattern of higher values in the west and lower values in the east. Specifically, the high-value center of SH is situated in the southern part of the Tianshan Mountains, located in the northwest of the TP, with a peak value of approximately 110 W/m^2. Conversely, the SH near the Kunlun Mountains in the western part of the TP is relatively low, falling below 10 W/m^2. In the central part of the TP, the SH generally averages around 40 W/m^2, with higher values observed in the northern TP and the Qaidam Basin, both exceeding 90 W/m^2. Notably, the Qaidam Basin shows a distinct spatial distribution characterized by higher values in the center and lower values around the edges (Figure 2a). The CMA-CPS predictions for June and July (Figure 2b,c) are generally consistent with the summer distribution, with SH hovering around 30 W/m^2 in most parts of the TP, except for the Tianshan Mountains, northern TP, and Qaidam Basin. The predicted SH for August shows a slight increase, with high-value areas concentrated in the Tianshan Mountains and Qaidam Basin (Figure 2d). Similarly, the CRA reanalysis data also show a spatial distribution of summer SH with higher values in the west and lower values in the east. On the TP, there are three high-value centers of summer SH: the Tianshan Mountains, the northern TP, and the vicinity of the Qaidam Basin. The highest values are recorded in the central and western parts of the northern TP, reaching up to 120 W/m^2, while the lowest values are around near the Kunlun Mountains, dipping to about 20 W/m^2 (Figure 2e). The SH distribution in June (Figure 2f) shows an overall increase compared to the summer, with particularly significant values in the northern TP, reaching up to 150 W/m^2. The SH distribution in July and August (Figure 2g,h) generally mirrors the summer average, with CRA values being overall higher than those of CMA-CPS. Specifically, the values in July are higher than the summer average, while the values in August are lower. In terms of relative variability, only a few areas of CMA-CPS's SH exceed 10%, whereas the areas with less than 10% variability in CRA are smaller and primarily located in the northern TP, indicating that the interannual variability of SH predicted by CMA-CPS is relatively modest.

The summer SH trends predicted by the CMA-CPS on the TP range between −10 and 10 W/m^2·(10a)$^{-1}$. Notably, there is a significant increase in the northern part of the TP, exceeding 10 W/m^2·(10a)$^{-1}$, albeit confined to a small area. Conversely, the surrounding regions show a significant decrease. The primary areas of increase are located in the northwest, northern, and southern TP, with trends around 5–10 W/m^2·(10a)$^{-1}$. Certain northern TP regions surpass the significance test (Figure 3a). The spatial distribution of SH trends predicted by the CMA-CPS for June and July generally aligns with the summer results, with differences primarily in the eastern TP. In June, the enhanced area in the southeastern TP is more extensive than during the summer, while in July, the

southeastern TP experiences a significant decrease. In August, there were no significant areas of increase in the northern TP, and the trend in the southern TP is decreasing, with the enhanced area in the eastern TP being larger than in summer (Figure 3b–d). The CRA reanalysis data also indicate an area of increase in the northern TP during summer, albeit with lesser intensity. The SH in the northeastern TP and west of 85°E exhibits an overall significant decrease, with the trends ranging from −5 to −15 $W/m^2 \cdot (10a)^{-1}$ in the former and exceeding −15 $W/m^2 \cdot (10a)^{-1}$ in the latter. The southern TP east of 85°E shows an overall increase (Figure 3e). The SH trend distribution in June is generally consistent with summer, but the weakening intensity in the Karakoram Mountains and northern TP exceeds 40 $W/m^2 \cdot (10a)^{-1}$, significantly stronger than in summer. In July, the area of significant decrease in the western TP is larger than in summer, whereas the decrease in the northeastern TP is smaller. In August, the area of increase in the central TP is more extensive than in other periods. The comparison reveals that the overall SH trend predicted by the CMA-CPS is smaller, aligning with the relative variability results in Figure 1, further indicating that the interannual variability of SH predicted by the CMA-CPS is relatively modest.

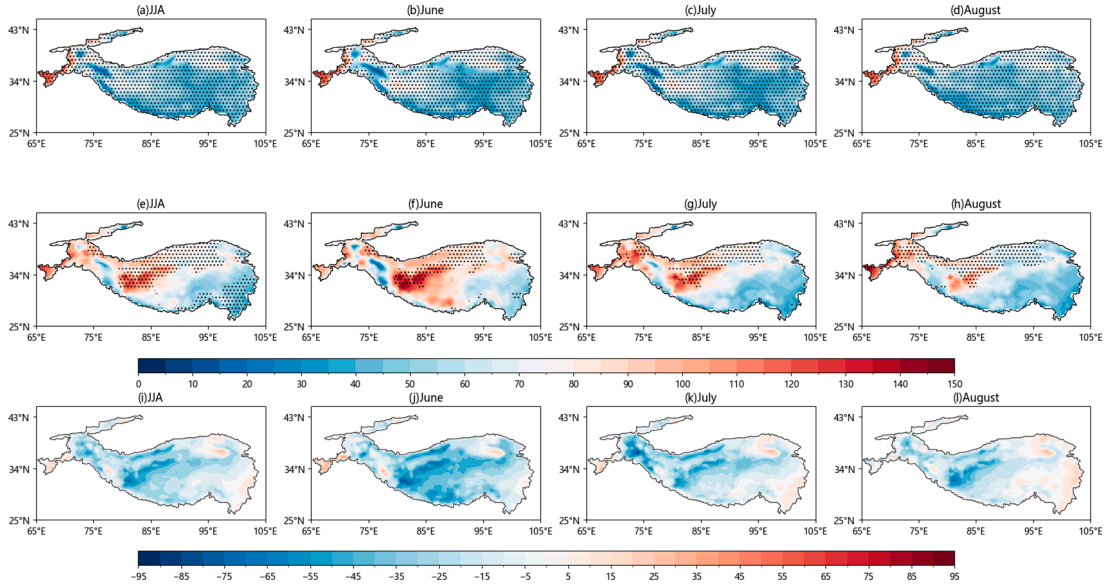


Figure 2. Spatial distribution of SH on the TP from CMA−CPS (**top**) and CRA (**middle**) from 2001 to 2021, and their differences (**bottom**) (unit: W/m^2). (**a**,**e**,**i**) Summer, (**b**,**f**,**j**) June, (**c**,**g**,**k**) July, (**d**,**h**,**l**) August. The dotted areas represent regions with a relative variability of 0–10%.

The *MAE* of SH predicted by CMA-CPS for the TP region in June is significantly higher than in other periods, with July and summer exhibiting comparable values and August recording the lowest. All periods display noticeable fluctuations. The *RRMSE* results are consistent with *MAE* (Figure 4a,b), indicating that the prediction bias of SH by CMA-CPS is the greatest in June and least in August. The proportion of years with high *ACC* scores (Figure 4c) is comparable for summer and June, at 15/21 and 16/21, respectively, followed by July (13/21), and August with the lowest proportion (10/21). This suggests that the spatial similarity between SH predicted by CMA-CPS and CRA is better in summer and June, especially in June 2008 and 2012, where the *ACC* values are exceptionally high, both exceeding 0.4, indicating a high level of agreement between CMA-CPS predictions and observed results for June SH on the TP in these years, with relatively superior prediction performance. The prediction performance in August shows significant fluctuations, with *ACC* values below 0 for more than half of the years, particularly in 2003 and 2014, where the *ACC* values in August are the lowest, below −0.2, further highlighting the need for improvement in prediction accuracy. As shown in Figure 4d, the proportion of years with high *TCC* scores from highest to lowest is August (19/21), summer (17/21), July

(16/21), and June (12/21). CMA-CPS demonstrates better predictive capability for grid point anomalies of SH in August and the worst in June. The *TCC* values for SH on the TP in August display relatively minor fluctuations, while the *TCC* values in June show substantial fluctuations, reflecting the sensitivity of SH predictions across different months. Overall, the *TCC* values for summer from 2009 to 2021 exhibit significant fluctuations, which may be attributed to the complexity and variability of the summer TP climate, making the prediction of SH on the TP more challenging.

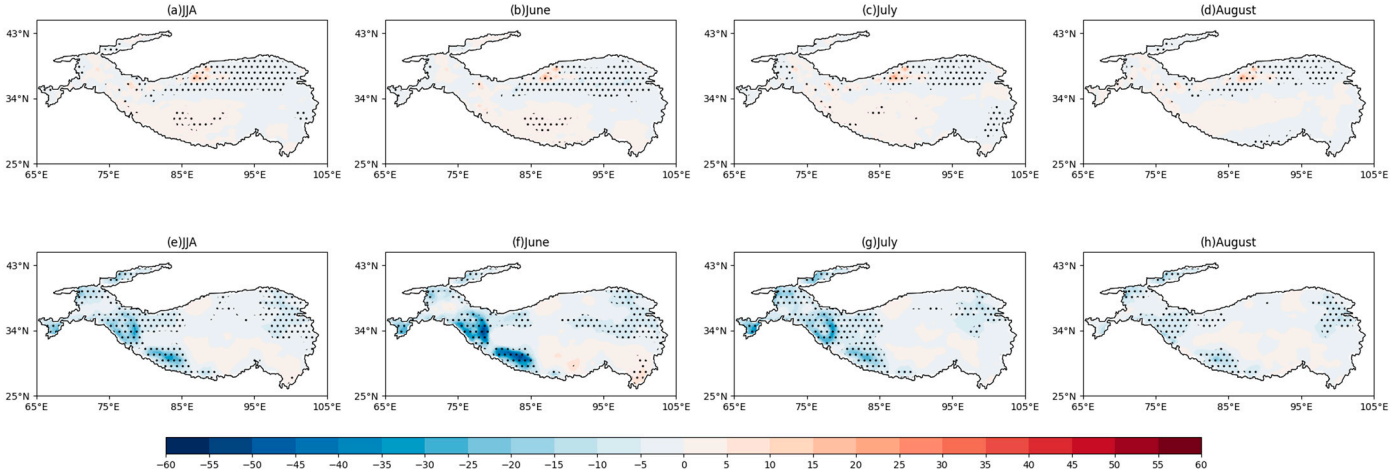


Figure 3. Spatial distribution of the climatic trend rate of SH on the TP from CMA−CPS (**top**) and CRA (**bottom**) from 2001 to 2021 (unit: $W/m^2 \cdot (10a)^{-1}$). (**a**,**e**) Summer, (**b**,**f**) June, (**c**,**g**) July, (**d**,**h**) August. The dotted areas indicate regions that passed the 90% significance test.



Figure 4. Time series of skill scores for SH on the TP predicted by CMA−CPS from 2001 to 2021. (**a**) *MAE*, (**b**) *RRMSE*, (**c**) *ACC*, (**d**) *TCC*.

The spatial distribution of *MAE* for SH predicted by CMA-CPS during different periods in summer shows conclusions consistent with Figure 4a. In summer, high-value areas are predominantly located in the Tianshan Mountains and the northern TP, with *MAE* values exceeding 60 W/m^2. Conversely, low-value areas are mainly concentrated in the

eastern TP, with specific regions in the Qaidam Basin and the southeastern TP exhibiting *MAE* values ranging from 0 to 5 W/m^2 (Figure 5a). In June, the high-value area of SH *MAE* extends from the northern TP to the southern side of the Qaidam Basin and the Gangdise Mountains, covering a significantly larger area compared to other periods. The spatial distribution of SH *MAE* in July mirrors that of summer, while in August, the high-value area in the northern TP diminishes compared to other periods, and the *MAE* in the central and eastern TP falls below 45 W/m^2 (Figure 5b–d). The spatial distribution of *RRMSE* for SH during different periods in summer is similar to that of *MAE*, with the primary distinction observed in the Karakoram Mountains, where the scope and values of the high *RRMSE* area are larger. Analyzing the spatial distribution of *ACC* scores for SH in summer (Figure 5i) reveals that the high-score areas are mainly in the northwestern TP, the Tanggula Mountains, and the northeastern TP. Conversely, the negative value areas are predominantly found in the northern TP and the Hengduan Mountains. The spatial distribution of *ACC* scores in June is similar to that of summer, but in June, the Hengduan Mountains exhibit high scores. In July, the high-score area is slightly narrow compared to summer and June, primarily located in the eastern TP, with the central TP largely featuring negative values. In August, the areas with positive and negative values are roughly equal, with positive values significantly smaller than in other periods (Figure 5j–l). The *MAE*, *RRMSE*, and *ACC* scores for SH during various summer periods show good temporal and spatial consistency, whereas the *TCC* scores are relatively weaker. The spatial distribution of *TCC* scores for SH across different periods remains similar, with high-score areas mainly in the northwestern and central-eastern TP. However, in June, the high-score area in the northern TP is significantly larger than in other periods, with minimal differences observed in other regions. Overall, the scoring effect is most favorable in June, followed by July and summer, with August demonstrating the least favorable outcomes (Figure 5m–p).

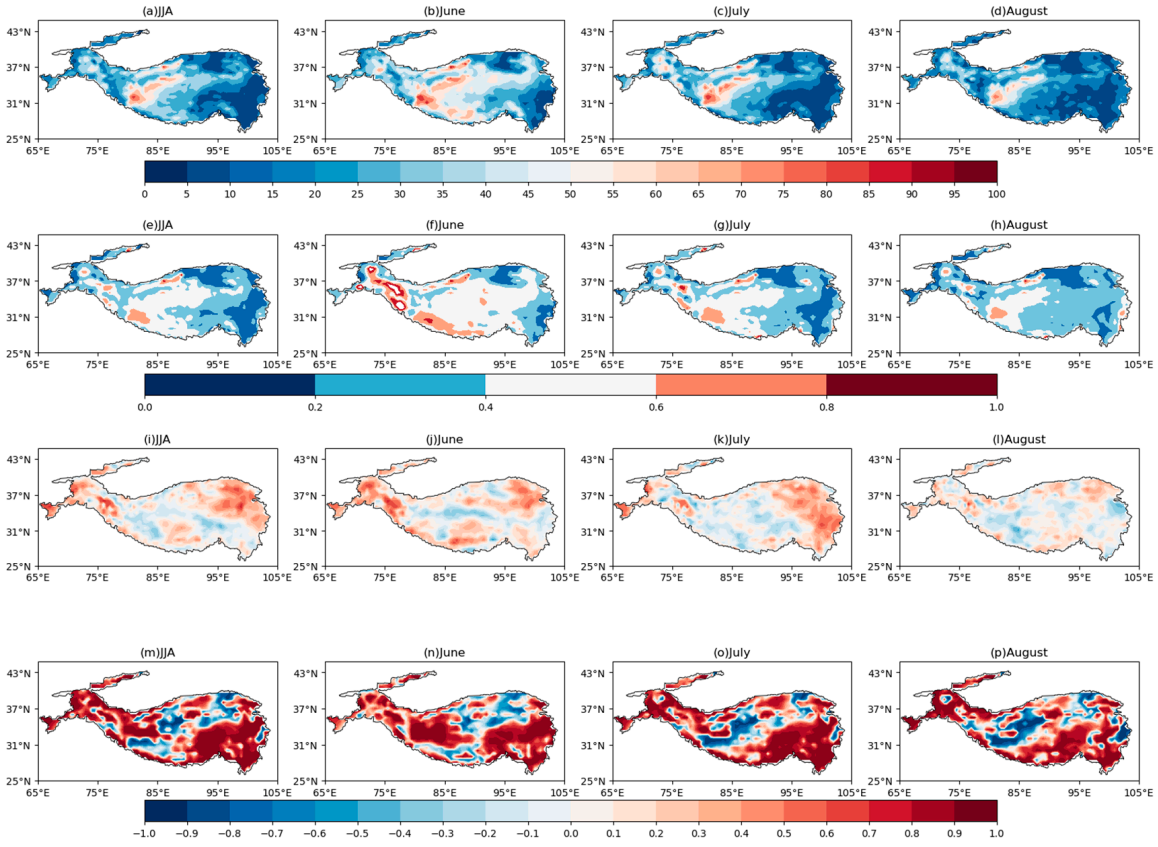


Figure 5. Spatial distribution of skill scores for SH on the TP predicted by CMA−CPS during different periods from 2001 to 2021. (**a**–**d**) *MAE*, (**e**–**h**) *RRMSE*, (**i**–**l**) *ACC*, (**m**–**p**) *TCC*.

3.3. Evaluation of Predictive Capability for LH

According to the CMA-CPS predictions, the spatial distribution of summer LH on the TP shows a pattern of higher values in the east and lower values in the west (Figure 6a). Specifically, the LH high-value center is located in the southeastern part of the TP, with a peak value approximating 100 W/m^2. Conversely, the LH in the northern TP is relatively low, less than 30 W/m^2, with the Karakoram Mountains and the Qaidam Basin exhibiting values of merely around 5 W/m^2. The distribution of LH predicted by CMA-CPS for June, July, and August (Figure 6b–d) is consistent with the summer distribution. Similarly, the CRA reanalysis data reveal a spatial distribution of summer LH that mirrors the east-high, west-low pattern, with the high-value area in the southeastern TP reaching up to 120 W/m^2 and the Qaidam Basin's low-value center dropping to approximately 5 W/m^2 (Figure 6e). In June, a decline in LH was observed in both the northern and southeastern TP compared to summer levels (Figure 6f). Conversely, in July and August, the LH in the southeastern TP increases compared to summer, with July exhibiting a more significant range and magnitude of increase. The spatial distribution of LH in August generally mirrors the summer pattern, with comparable values (Figure 6g,h). Overall, the LH values derived from CRA are higher than those from CMA-CPS. The areas where CMA-CPS predictions exceed actual values are in the northern TP, with June experiencing a significantly larger range of overestimation compared to other periods. In terms of relative variability, areas with less than 10% variability are mainly located in the high-value areas for both CMA-CPS and CRA. However, the range is broader for CMA-CPS, indicating that the interannual variability of LH predicted by CMA-CPS is relatively smaller.

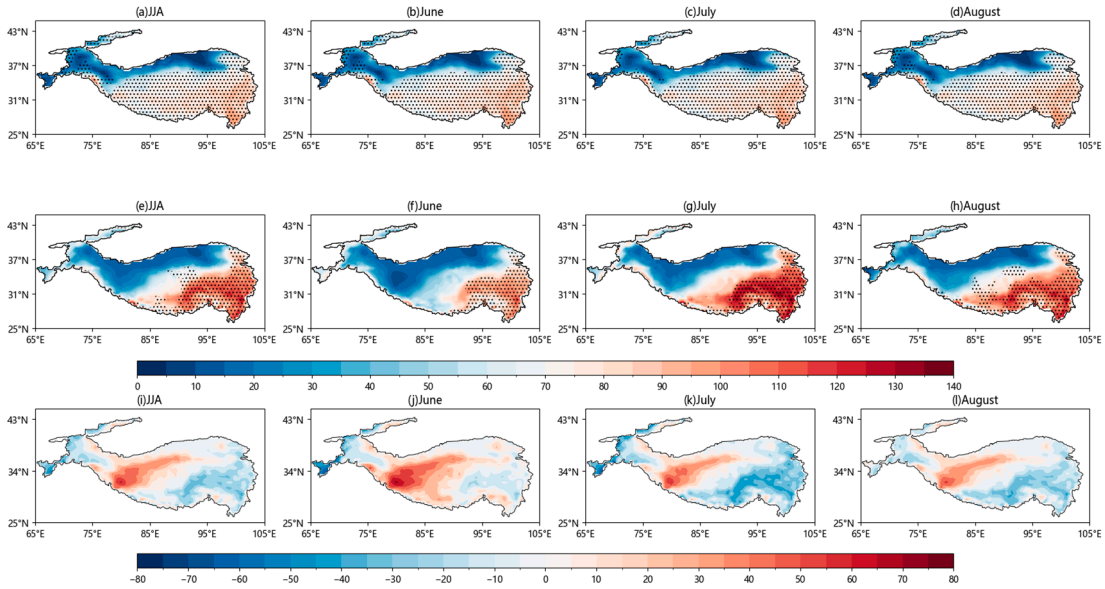


Figure 6. Spatial distribution of LH on the TP from CMA−CPS (**top**) and CRA (**middle**) from 2001 to 2021, and their differences (**bottom**) (unit: W/m^2). (**a**,**e**,**i**) Summer, (**b**,**f**,**j**) June, (**c**,**g**,**k**) July, (**d**,**h**,**l**) August. The dotted areas represent regions with a relative variability of 0–10%.

The trend of summer LH on the TP predicted by CMA-CPS ranges from −5 to 15 $W/m^2 \cdot (10a)^{-1}$, indicating an overall increasing trend. Notably, the regions experiencing significant increases are concentrated primarily in the northern TP, whereas decreases are also observed, albeit predominantly in the northern TP (Figure 7a). The spatial distribution of LH trends in June, July, and August mirrors that of summer, with the notable exception of discrepancies in the distribution of significantly increased areas in the southeastern TP (Figure 7b–d). According to the CRA reanalysis data, the overall trend of summer LH on the TP also shows an increasing trend, with significant increments in the western and northeastern TP, peaking at 40 $W/m^2 \cdot (10a)^{-1}$. Conversely, decreases are observed mainly in the southeastern TP, with values hovering around 0–5 $W/m^2 \cdot (10a)^{-1}$ (Figure 7e). In June

and August, the trend of LH in the northern TP is weaker compared to summer, while in July and August, the trend in the northeastern TP is similarly subdued relative to the summer trend (Figure 7f–h). Comparatively, the trend of LH predicted by CMA-CPS is generally smaller than that of CRA, with significant differences in the central locations.

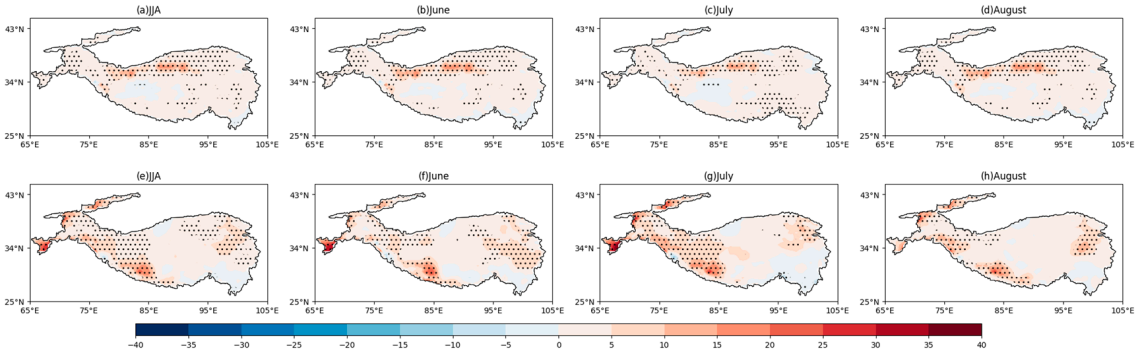


Figure 7. Spatial distribution of the climatic trend rate of LH on the TP from CMA−CPS (**top**) and CRA (**bottom**) from 2001 to 2021 (unit: $W/m^2 \cdot (10a)^{-1}$). (**a**,**e**) Summer, (**b**,**f**) June, (**c**,**g**) July, (**d**,**h**) August. The dotted areas indicate regions that passed the 90% significance test.

Figure 8 presents the predictive capabilities of CMA-CPS for LH over the TP during various summer periods, evaluated through diverse scoring methodologies. The *MAE* for LH predictions in July surpasses that of other periods, generally ranging between 25 and 30 W/m^2, with only 2001 exhibiting an *MAE* below 25 W/m^2. June and summer predictions are comparable, while August boasts the lowest *MAE* values, all showing noticeable fluctuations. Similarly, the *RRMSE* mirrors the *MAE* trends, with June's *RRMSE* surpassing summer's in certain years from 2005 to 2016, showing significant fluctuations (Figure 8a,b). This indicates that the prediction bias for LH by CMA-CPS is the most pronounced in July and the smallest in August. The proportion of years achieving high *ACC* scores is 14/21 for summer, 15/21 for June, 13/21 for July, and 15/21 for August, indicating that the spatial similarity of LH predicted by CMA-CPS is comparable across these periods (Figure 8c). Notably, *ACC* values for June and summer in 2001 and 2012, as well as for August in 2012, 2018, and 2019, are exceptionally close to 0.4, indicating relatively superior prediction performance during these years. Conversely, all *ACC* values for 2021 across periods are negative, with June and summer dipping below −0.2, highlighting a need for performance enhancement. While the proportion of years achieving high *TCC* scores reaches 100% across periods, June's score is lower, indicating that CMA-CPS's predictive prowess for grid point anomalies of latent heat in June is poor and requires improvement, with fluctuations in other periods remaining relatively small.

The high-*MAE* zones for summer LH predicted by CMA-CPS are concentrated in the western Tianshan Mountains, northern TP, and southeastern TP (figure omitted). In June and July, LH *MAE* values in the northern and eastern TP soar up to 80 W/m^2, with the high-value area on the western side of the Tianshan Mountains in July being significantly larger than in June. The overall *MAE* in August is lower than in summer, with only the northern TP nearing 50 W/m^2. The spatial distribution of LH *RRMSE* aligns with *MAE*. Summer LH *ACC* scores feature negative values only in the northern TP and southern Tianshan Mountains, with the rest of the TP scoring high, indicating a good spatial similarity between CMA-CPS predictions and observed LH values. The *ACC* spatial distribution in June, July, and August resembles summer's, with fewer negative value areas in June compared to summer, while July and August exhibit similar but more extensive negative areas. The overall high scores in August are lower, indicating poorer spatial similarity of LH compared to other periods. Negative *TCC* score areas for LH are primarily located in the northern TP, with the size of these areas for each period consistent with the scoring effect in Figure 8d. The remaining regions score high, indicating good predictive ability of CMA-CPS for grid point anomalies of LH on the TP overall, albeit with weaker performance in the northern TP.



Figure 8. Time series of skill scores for LH on the TP predicted by CMA−CPS from 2001 to 2021. (**a**) *MAE*, (**b**) *RRMSE*, (**c**) *ACC*, (**d**) *TCC*.

3.4. Evaluation of Predictive Capability for SHS

In Figure 9, the spatial distribution pattern of the predicted SHS on the TP is consistent with that of LH in summer. The low-value areas of the predicted SHS are located in the northern TP and the Qaidam Basin, with the lowest values in the northern TP reaching 5 W/m^2. The predicted SHS in the northern TP is around 80 W/m^2, whereas, in other regions, the values are approximately 120 W/m^2. The predicted SHS in the southern Qaidam Basin is lower than that in summer, June, and July and lower in the western northern TP in August. The spatial distribution of SHS from CRA is consistent with that from CMA-CPS, but the overall SHS values are higher, with the center of the high-value area reaching up to 180 W/m^2 and the low-value area down to 40 W/m^2. The relative variability of SHS on the TP for both CMA-CPS and CRA is generally below 10%, possibly because the SHS is derived through direct algorithms and the opposing trends of SH and LH offset each other, weakening the trend.

The scoring results for the predicted SHS are as follows: *MAE* and *RRMSE* are similar to the results for LH in time and space. The proportion of years with high *ACC* scores is best in June (15/21), similar in July (12/21) and August (12/21), and worst in summer (10/21). The high-score areas for SHS in summer, July, and August are significantly larger than the negative value areas, mainly located in the Tianshan Mountains, Karakoram Mountains, and northern TP, while in June, the negative value areas are more numerous, mainly in the central TP. The proportion of years with high *TCC* scores for SHS is consistent with LH, with overall values above 0.6.

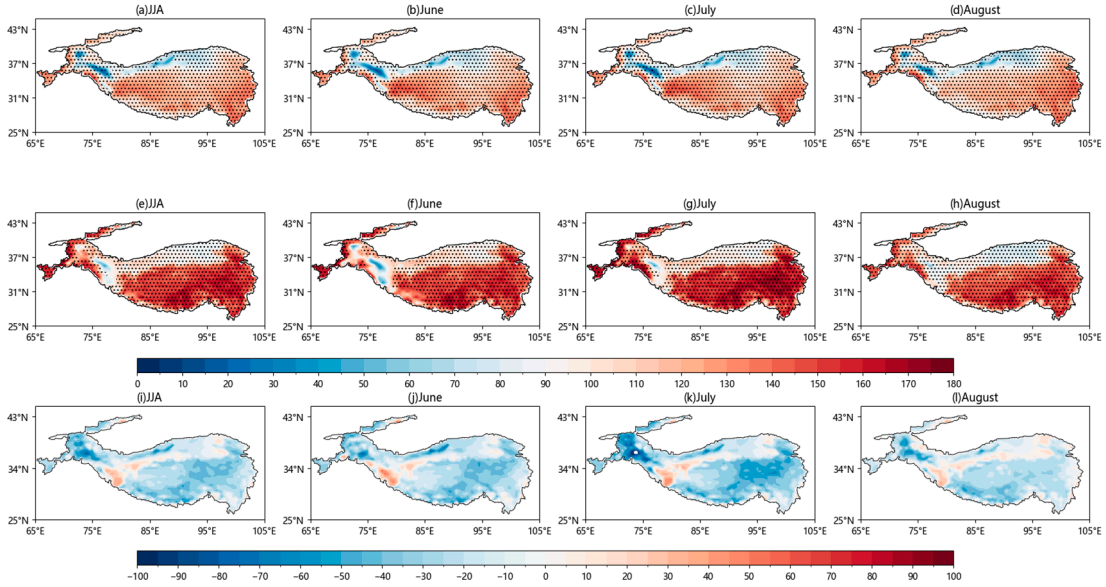


Figure 9. Spatial distribution of SHS on the TP (unit: W/m^2) from CMA−CPS (**top**) and CRA (**middle**) from 2001 to 2021, and their differences (**bottom**). (**a**,**e**,**i**) Summer, (**b**,**f**,**j**) June, (**c**,**g**,**k**) July, (**d**,**h**,**l**) August. The dotted areas represent regions with a relative variability of 0–10%.

4. Discussion

Many studies have shown that the temperature difference between the ground and the atmosphere, surface wind speed, and humidity on the TP have a significant impact on SH and LH [10–16,51,52]. To preliminarily explore the reasons for CMA-CPS's prediction bias, an initial assessment of the temperature difference between the ground and the atmosphere, surface wind speed, and specific humidity on the TP was conducted for both CMA-CPS and CRA.

This study highlights significant variations in SH across the Tibetan Plateau TP, with distinct factors influencing each region. Notably, the elevated SH levels recorded in the eastern TP may stem from an overestimation of surface wind speed, which, when combined with a pronounced temperature differential between the ground and the atmosphere, likely contributes to these high values. In contrast, the lower SH observed in the central TP can be attributed to an underestimation of surface wind speed, suggesting a need for refined measurements in this area. Furthermore, the diminished SH in the western TP appears to be closely associated with an underestimation of the temperature differential between the ground and the atmosphere, as illustrated in Figure 10a–h. In addition to these regional disparities, the spatial distribution map of specific humidity differences, predicted by the CMA-CPS, reveals a complementary pattern: elevated values in the west and reduced values in the east. This spatial distribution closely aligns with the LH differences presented in Figure 10i–l, indicating a correlation that warrants further investigation to elucidate the underlying mechanisms responsible for these observations. Moreover, several characteristics of the TP's underlying surface significantly influence heat dynamics and contribute to the complexity of SH variations. For instance, changes in snow cover, alongside feedback mechanisms related to ice and snow albedo, can markedly alter surface temperature fluctuations across the region. Additionally, shifting permafrost conditions further complicate the thermal dynamics at the surface. Furthermore, surface vegetation exerts a dual influence on SH. It not only mitigates heat penetration into the shallow soil, resulting in lower surface temperatures, but also contributes to a reduction in surface wind speed. Therefore, a comprehensive examination of these underlying surface factors is essential for gaining a nuanced understanding of the observed variations in SH and their broader climatic implications for the TP.

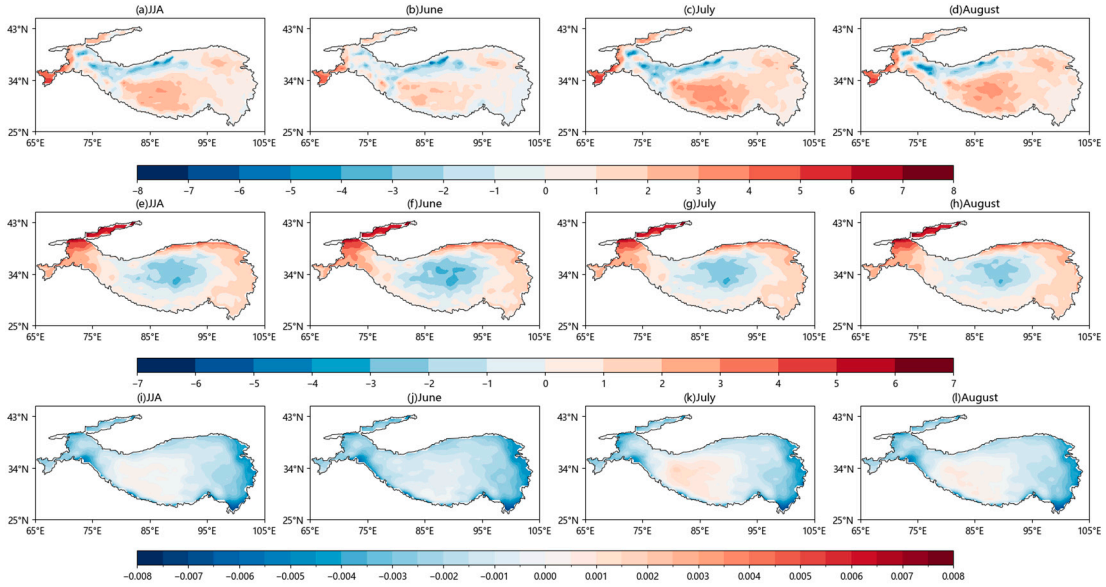


Figure 10. Spatial distribution of the differences in ground-air temperature (**top**), surface wind speed (**middle**), and specific humidity (**bottom**) on the TP as predicted by CMA−CPS and reanalyzed by CRA for different periods from 2001 to 2021 (units: °C, m/s, kg/kg, respectively). (**a**,**e**,**i**) Summer, (**b**,**f**,**j**) June, (**c**,**g**,**k**) July, (**d**,**h**,**l**) August.

Although the predictive capability of the CMA-CPS for SHS and their components in the summer over the TP has been systematically evaluated from the perspectives of bias, spatial similarity, and trend variation, the complex geographical environment of the TP prevents the use of observational station data for evaluation. We look forward to the establishment of more observational stations in the future to improve the model's predictive capability.

5. Conclusions

SHS data from eleven observation stations on the Tibetan Plateau TP and CRA reanalysis data were utilized to systematically evaluate the CMA-CPS's ability to predict summer SHS on the TP. The following main conclusions were drawn.

Both CRA and ERA5 reanalysis data exhibited similar correlations with observational data; however, CRA showed less dispersion. Therefore, CRA was selected as the comparative dataset.

The CMA-CPS predicted summer SH distribution on the TP revealed a pattern of high values in the west and lower values in the east, contrasting with LH, which displayed higher values in the east and lower values in the west. The SHS closely resembled LHt and aligned well with CRA results, indicating that CMA-CPS effectively captured the spatial distribution characteristics of SHS and its components on the TP during summer, albeit with predicted values approximately 25 W/m^2 lower.

Overall trends for SH and LH predicted by CMA-CPS were found to be −10 to 10 $W/m^2 \cdot (10a^{-1})$ and −5 to 15 $W/m^2 \cdot (10a^{-1})$, respectively. In comparison, CRA indicated a more pronounced weakening trend in SH > 15 $W/m^2 \cdot (10a^{-1})$ and a broader area of significant enhancement in LH. This suggests that trends predicted by CMA-CPS are smaller than those from CRA, which may account for the lesser interannual variability observed. Minimal interannual variations in SHS on the TP were shown by both CMA-CPS and CRA, likely due to the direct calculation of SHS leading to offsetting trends between SH and LH.

Among the predictions, LH demonstrated the highest overall skill, followed by SHS, while SH exhibited the lowest skill. Significant deviations in SH were observed in June and minimal deviations in August, especially in northern TP regions. Spatial similarity was highest during summer and in June, decreasing in August. For LH, the largest prediction

deviations occurred in July, with significant discrepancies noted in northern and eastern TP. Approximately two-thirds of the years showed good *ACC* scores for LH, predominantly in the eastern and western TP, while *TCC* scores were consistently high, except in the northern TP. These results indicated that LH contributed more substantially to summer TP SHS than SH itself.

The prediction biases for SH and LH by CMA-CPS arose from different causes. The high bias in SH in the eastern TP was attributed to overestimated surface wind speed and ground-air temperature differences, while the low bias in the central TP resulted from underestimated surface wind speed. In the western TP, low ground-air temperature differences led to a low bias in SH. The spatial distribution of specific humidity discrepancies aligned with that of LH, suggesting that the prediction bias in specific humidity by CMA-CPS indirectly affected its LH prediction capability.

After a systematic evaluation, it has been determined that the predictive capability of the CMA-CPS for SHS and its components during the summer on the TP requires further improvement. The potential causes for this bias have been preliminarily discussed, highlighting the need for a more comprehensive evaluation of CMA-CPS's ability to predict the underlying surface factors of the TP. Such an assessment would provide a theoretical basis for enhancing the model's accuracy.

Author Contributions: Writing—original draft, X.C.; writing—review and editing, M.S., Y.W. and T.W. All authors have read and agreed to the published version of the manuscript.

Funding: This research was supported by the Second Tibetan Plateau Scientific Expedition and Research Program (STEP) (NO. 2019QZKK0103) and the National Natural Science Foundation of China, grant number: 42230608.

Data Availability Statement: The CRA40-land and ERA5-land datasets are available from the following sources: the CRA40-land dataset can be accessed from http://www.nmic.cn/ (accessed on 12 January 2024), and the ERA5-land dataset can be obtained from https://cds.climate.copernicus.eu/ (accessed on 12 January 2024).

Conflicts of Interest: The authors declare no conflict of interest.

References

1. Zhou, X.J.; Zhao, P.; Chen, J.M.; Chen, L.X.; Li, W.L. Impacts of thermodynamic processes over the Tibetan Plateau on the Northern Hemispheric climate. *Sci. China Ser. D Earth Sci.* **2009**, *52*, 1679–1693. [CrossRef]
2. Ma, Y.; Hu, Z.Y.; Tian, L.D.; Zhang, F.; Duan, A.; Yang, K.; Zhang, Y.; Yang, Y. Progress in research on climate system changes over the Tibetan Plateau and their impacts and mechanisms on the East Asian region. *Adv. Earth Sci.* **2014**, *29*, 207–215.
3. Duan, A.; Sun, R.; He, J. Impact of surface sensible heating over the Tibetan Plateau on the western Pacific subtropical high: A land–air–sea interaction perspective. *Adv. Atmos. Sci.* **2017**, *34*, 157–168. [CrossRef]
4. Ma, Y.; Ma, W.; Zhong, L.; Hu, Z.; Li, M.; Zhu, Z.K.; Han, C.; Wang, B.; Liu, X. Monitoring and Modeling the Tibetan Plateau's climate system and its impact on East Asia. *Sci. Rep.* **2017**, *7*, 44574. [CrossRef]
5. Duan, A.; Liu, Y.; Wu, G. The thermal conditions over the Tibetan Plateau from April to June and the anomalies of summer precipitation and atmospheric circulation in East Asia. *Earth Sci. Ser. D* **2003**, *33*, 997–1004.
6. Duan, A.; Wu, G. Weakening trend in the atmospheric heat source over the Tibetan Plateau during recent decades. Part I: Observations. *J. Clim.* **2008**, *21*, 3149–3164. [CrossRef]
7. Zhong, S.; He, J.; Guan, Z.; Wen, M. Climatic characteristics of atmospheric heat sources over the Tibetan Plateau from 1961 to 2001. *Acta Meteorol. Sin.* **2009**, *67*, 407–416.
8. Wang, M.; Guo, D.; Zhong, S. Applicability analysis of multi-source data in calculating atmospheric heat sources over the Tibetan Plateau. *Meteorology* **2019**, *45*, 1718–1726.
9. Ma, Y.; Hu, Z.; Wang, B.; Ma, W.; Chen, X.; Han, C.; Li, M.; Zhong, L.; Gu, L.; Sun, F.; et al. Progress and review of research on multi-sphere land-atmosphere interaction processes over the Tibetan Plateau. *Plateau Meteorol.* **2021**, *40*, 1241–1262.
10. Yu, W.; Liu, Y.; Yang, X.; Wu, G. Interannual and decadal variation characteristics and causes of surface sensible heat at different altitudes on the Tibetan Plateau. *Plateau Meteorol.* **2018**, *37*, 1161–1176.
11. Lei, R.; Yu, Y.; Zhou, G.; Li, J.; Liu, Y. Long-term trend analysis of sensible heat flux over the Tibetan Plateau from 1984 to 2020. *Plateau Meteorol.* **2023**, *42*, 833–847.
12. Wang, H.; Zhang, L.; Shi, X.; Li, D. Seasonal differences in the turning characteristics of surface sensible heat trends in central and eastern Tibetan Plateau. *Chin. J. Atmos. Sci.* **2022**, *46*, 133–150.

13. Yang, K.; Guo, X.F.; Wu, B.Y. Recent trends in surface sensible heat flux on the Tibetan Plateau. *Sci. China Earth Sci.* **2011**, *54*, 19–28. [CrossRef]
14. Yang, L.; Zhang, Q. Analysis of circulation and surface latent heat flux characteristics of summer precipitation anomalies in southern Xinjiang. *Plateau Meteorol.* **2007**, *26*, 435–441.
15. Yu, L.; Chen, H. Relationship between April land surface conditions and surface heating anomalies on the Tibetan Plateau and summer precipitation in China. *Plateau Meteorol.* **2012**, *31*, 1173–1182.
16. Qi, Y.; Yan, Y.; Li, J.; Chen, W. Relationship between surface latent heat flux from May to October on the Tibetan Plateau and precipitation in Qinghai during the same period. *Arid Zone Res.* **2019**, *36*, 529–536. [CrossRef]
17. Wang, Z.; Li, G. Diagnostic analysis of a nighttime rainstorm on the eastern slope of the Tibetan Plateau based on heat source effects. *Desert Oasis Meteorol.* **2023**, *17*, 96–103.
18. Li, Y.; Gao, X.; Ma, Y.; Hu, Z.; Li, Z.; Yang, L.; Jin, X.; Zhou, Y. Atmospheric heat engine efficiency and heat source characteristics over the Tibetan Plateau in summer. *Sci. China Earth Sci.* **2024**, *54*, 122–137.
19. Chen, L.; Pryor, S.C.; Wang, H.; Zhang, R. Distribution and variation of the surface sensible heat flux over the central and eastern Tibetan Plateau: Comparison of station observations and multireanalysis products. *J. Geophys. Res. Atmos.* **2019**, *124*, 6191–6206. [CrossRef]
20. Wu, Z.; Chen, Q. Comparative analysis of surface sensible heat on the Tibetan Plateau based on multiple data sources. *Plateau Mt. Meteorol. Res.* **2018**, *38*, 1–10.
21. Zhong, L.; Ma, Y.; Hu, Z.; Fu, Y.; Hu, Y.; Wang, X.; Cheng, M.; Ge, N. Estimation of hourly land surface heat fluxes over the Tibetan Plateau by the combined use of geostationary and polar-orbiting satellites. *Atmos. Chem. Phys.* **2019**, *19*, 5529–5541. [CrossRef]
22. Zhong, L.; Ge, N.; Ma, Y.; Fu, Y.; Ma, W.; Han, C.; Wang, X.; Cheng, M. Estimation of surface latent heat flux over the entire Tibetan Plateau using geostationary satellites. *Adv. Earth Sci.* **2021**, *36*, 773–784.
23. Ma, Y.; Zhong, L.; Wang, B.; Ma, W.; Chen, X.; Li, M. Determination of land surface heat fluxes over heterogeneous landscape of the Tibetan Plateau by using the MODIS and in situ data. *Atmos. Chem. Phys.* **2011**, *11*, 10461–10469. [CrossRef]
24. Hua, W.; Lin, Z.; Guo, D.; Fan, G.; Zhang, Y.; Yang, K.; Hu, Q.; Zhu, L. Simulated long-term vegetation–climate feedbacks in the Tibetan Plateau. *Asia-Pac. J. Atmos. Sci.* **2019**, *55*, 41–52. [CrossRef]
25. Zhang, S.; Chen, Y.; Lü, S.; Li, S.; Wang, S.Y. Simulation study on the impact of vegetation changes on the Tibetan Plateau on summer precipitation in eastern China. *Plateau Meteorol.* **2013**, *32*, 1236–1245.
26. Chen, J.; Wu, X.; Yin, Y.; Lu, C.; Xiao, H.; Huang, Q.; Deng, L.P. Thermal effects of the surface heat flux on cloud systems over the Tibetan Plateau in boreal summer. *J. Clim.* **2019**, *32*, 4699–4714. [CrossRef]
27. Li, M.; Yin, S.; Liu, X.; Liu, X.; Lü, Z.; Song, X.; Ma, Y.; Sun, F. Numerical simulation of turbulent flux changes over the Tibetan Plateau and its surroundings in the past decade. *Plateau Meteorol.* **2019**, *38*, 1140–1148.
28. Hu, W.; Ma, W.; Ma, Y.; Xie, Z. Evaluation of the simulation performance of the Noah-MP land surface model driven by GLDAS data on surface energy exchange over the Tibetan Plateau. *Plateau Meteorol.* **2020**, *39*, 486–498.
29. Xie, Z.; Hu, Z.; Liu, H.; Sun, G.; Yang, Y.; Lin, Y.; Huang, F. Evaluation of the simulation performance of the CLM4.5 land surface model on surface energy exchange over alpine meadows on the Tibetan Plateau. *Plateau Meteorol.* **2017**, *36*, 1–12.
30. Wang, S.; Ma, Y.; Wu, W. Distribution and variation characteristics of surface sensible and latent heat fluxes on the Tibetan Plateau based on the Noah-MP land surface model. *Plateau Meteorol.* **2023**, *42*, 25–34.
31. Wu, T. *Integrated Climate Model Prediction System on Sub-Seasonal to Seasonal to Interannual Scales (CMA-CPS)*; National Climate Center: Beijing, China, 29 August 2022.
32. Li, Y.; Zhu, R.; Liu, T.; Chang, Y.; Yin, Z. Analysis of future temperature and precipitation trends in the Shule River Basin based on the BCC-CSM2-MR model. *Plateau Meteorol.* **2021**, *40*, 535–546.
33. Zhai, Q.; Sun, F.; Ao, X.; Geng, S.; Li, C.; Li, Y.; Li, M. Simulation and prediction of temperature and precipitation in the Liao River Basin based on the BCC-CSM2-MR model CMIP6 experiment. *J. Meteorol. Environ.* **2022**, *38*, 27–36.
34. Zhang, Z.; Zhou, F.; Zhang, H.; Zhou, C.; Wang, X. Evaluation of the prediction of typical winter circulation systems by BCC_CSM1.1m. *J. Appl. Meteorol.* **2023**, *34*, 27–38.
35. Li, S.; Quan, W.; Wang, Z.; Chen, Y.; Su, T.; Yan, P. Evaluation of BCC-CSM2-MR Global Climate Model Simulation of Precipitation and Temperature in East Asia. *Arid Meteorol.* **2023**, *41*, 984–996.
36. Song, M.; Pei, Y.; Zhang, S.; Wu, T. Simulation Performance and Case Study of Extreme Events in Northwest China Using the BCC-CSM2 Model. *Remote Sens.* **2022**, *14*, 4922. [CrossRef]
37. Xue, J.; Shan, H.; Liang, J.H.; Dong, C.M. Assessment and Projections of Marine Heatwaves in the Northwest Pacific Based on CMIP6 Models. *Remote Sens.* **2023**, *15*, 2957. [CrossRef]
38. Liu, J.; Lu, Y. How well do CMIP6 models simulate the greening of the Tibetan Plateau? *Remote Sens.* **2022**, *14*, 4633. [CrossRef]
39. Zhang, H.; Liang, X.; Wang, F.; Xie, B.; Li, Q. Improvement of BCC_CSM1.1m's Cross-Seasonal Dynamic Prediction Capability for Summer Precipitation in China by CWRF Downscaling. *J. Atmos. Sci.* **2023**, *46*, 161–179. [CrossRef]
40. Ying, W.; Yan, H.; Luo, J.J. Seasonal predictions of summer precipitation in the middle-lower reaches of the Yangtze River with global and regional models based on NUIST-CFS1.0. *Adv. Atmos. Sci.* **2022**, *39*, 1561–1578. [CrossRef]
41. Gu, B.; Zheng, Z.; Feng, G.; Wang, Z. The capacity of seasonal forecast models for the forecast of the East Asian summer circulation and its response to tropical SST anomaly. *Chin. J. Atmos. Sci.* **2017**, *41*, 91–105. (In Chinese) [CrossRef]

42. Liang, P.; Lin, H. Sub-seasonal prediction over East Asia during boreal summer using the ECCC monthly forecasting system. *Clim. Dyn.* **2018**, *50*, 1007–1022. [CrossRef]
43. Li, J.; Zhu, Z.; Dong, W. Assessing the uncertainty of CESM-LE in simulating the trends of mean and extreme temperature and precipitation over China. *Int. J. Climatol.* **2017**, *37*, 2101–2110. [CrossRef]
44. Jie, W.; Vitart, F.; Wu, T.; Wu, T.; Liu, X.W. Simulations of the Asian summer monsoon in the sub-seasonal to seasonal prediction project (S2S) database. *Q. J. R. Meteorol. Soc.* **2017**, *143*, 2282–2295. [CrossRef]
45. Ma, Y.; Xie, Z.; Chen, Y.; Liu, S.; Che, T.; Xu, Z.; Shang, L.; He, X.; Meng, X.; Ma, W.; et al. Dataset of spatially extensive long-term quality-assured land–atmosphere interactions over the Tibetan Plateau. *Earth Syst. Sci. Data* **2024**, *16*, 3017–3043. [CrossRef]
46. Xin, X.; Wu, T.; Zhang, J.; Zhang, F.; Li, W.; Zhang, Y.; Lu, Y.; Fang, Y.; Jie, W.; Zhang, L.; et al. Introduction to BCC Model and Its CMIP6 Experiments. *Adv. Clim. Change Res.* **2019**, *15*, 533–539.
47. Li, G.; Lu, H.; Huang, C.; Fan, Y.; Zhang, B. Climatic Characteristics of Summer Surface Heat Source on the Tibetan Plateau and Its Impact on the Formation of Plateau Vortices. *J. Atmos. Sci.* **2016**, *40*, 131–141.
48. Wu, J.; Ren, H.; Zhang, S.; Liu, Y.; Liu, X. Seasonal Prediction Evaluation and Predictability Analysis of the Second Generation BCC Climate System Model. *J. Atmos. Sci.* **2017**, *41*, 1300–1315.
49. Abdolmanafi, A.; Saghafian, B.; Aminyavari, S. Evaluation of Global Ensemble Prediction Models for Forecasting Medium to Heavy Precipitations. *Meteorol. Atmos. Phys.* **2021**, *133*, 15–26. [CrossRef]
50. Li, N. Calculation and Variability Study of Surface Heat Source on the Tibetan Plateau. Ph.D. Thesis, Chinese Academy of Meteorological Sciences, Beijing, China, 2020. [CrossRef]
51. Wang, C.; Shi, R. Simulation Analysis of Land Surface Process Characteristics in Western Tibetan Plateau. *J. Glaciol. Geocryol.* **2007**, *29*, 73–81.
52. Tan, J.; Huang, A.; Shi, X.; Zhang, Y.; Zhang, Y.; Cao, L.; Wu, Y. Evaluation of BCC-CSM2-MR Model's Simulation Capability for Land Surface Processes in China. *Plateau Meteorol.* **2022**, *41*, 1335–1347.

Disclaimer/Publisher's Note: The statements, opinions and data contained in all publications are solely those of the individual author(s) and contributor(s) and not of MDPI and/or the editor(s). MDPI and/or the editor(s) disclaim responsibility for any injury to people or property resulting from any ideas, methods, instructions or products referred to in the content.